# The Black Hole of Water Vapor and the Asymmetries in the Tropical Circulation

Takamitsu Ito*

## 1 Introduction

The water vapor (hereafter, WV) satellite images comes from the long wave channel of wavelength 5.7–7.1 [$\mu m$]. Images of the earth at these wavelengths do not show any surface features of the earth, since the radiation emitted by the earth's surface at that wave length is entirely absorbed by low-level atmospheric WV. The features that these images reveal are related to planetary scale and synoptic scale variations of WV in the middle and upper troposphere.

Figure 1 is an upper tropospheric WV image taken during the northern hemisphere summer *(obtained from http://kauai.nrlmry.navy.mil/sat-bin/global.cgi)*. Intertropical Convergence Zone (ITCZ) is rich in moisture and is located at approximately 8 degrees latitude. Outside of the narrow band of ITCZ, the air is relatively dry, especially in the winter hemisphere. In Figure 1, there is a region of very low humidity in the tropical Eastern Pacific. It is the "Black Hole" of water vapor in the south of the equator about the same latitude as ITCZ.

Observational studies *[Picon and Desbios [7]; Schmez et al. [9]]* have shown the statistical correlation between the divergence of the large scale circulation and the satellite WV observations. In subsidence conditions, the upper troposphere become dry and the 5.7–7.1 [$\mu m$] radiation received by the satellite comes primarily from the relatively warm mid-troposphere. When the large-scale vertical motion is upward, the upper troposphere could become nearly saturated, and the 5.7–7.1 [$\mu m$] radiation comes from the relatively cold upper troposphere. In this way the "equivalent blackbody temperature" of the 5.7–7.1 [$\mu m$] radiation is a proxy for the vertical motion field. Since the vertical motion field is not directly measurable by any meteorological instrument, WV images can be an useful tool to diagnose the vertical velocity.

The size and the location of the Black Hole is not homogeneous in time and space. The extent and the intensity of the dry region is much greater in the winter hemisphere. The Black Hole tends to appear in the winter hemisphere of approximately the same latitude as the location of the deep convection in ITCZ. These features appears and disappears on the time scale of a few days to a few weeks. Figure 1 is the WV image over the Eastern Pacific from GOES-10. The Black Hole is formed over the Tropical Pacific in the late July,

*with Edwin P. Gerber and Wayne H. Schubert

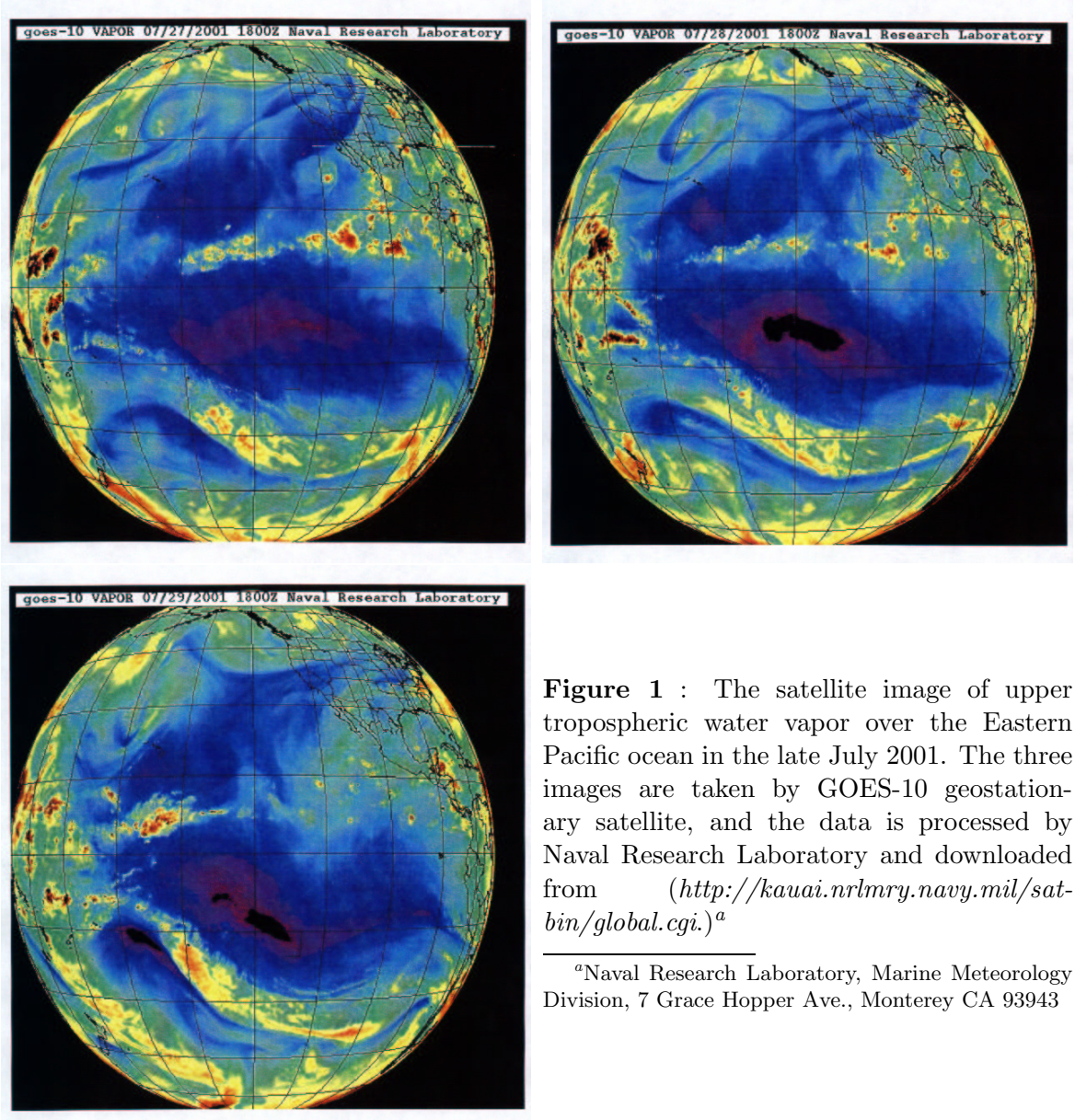


**Figure 1** : The satellite image of upper tropospheric water vapor over the Eastern Pacific ocean in the late July 2001. The three images are taken by GOES-10 geostationary satellite, and the data is processed by Naval Research Laboratory and downloaded from (*http://kauai.nrlmry.navy.mil/satbin/global.cgi.*)[a]

[a]Naval Research Laboratory, Marine Meteorology Division, 7 Grace Hopper Ave., Monterey CA 93943

2001. What controls the spatial structure and intensity of the Black Hole ? Could we use a simple theory to explain these phenomena ?

This study is an attempt to understand the mechanisms which determines the structure of the Black Hole in the tropical atmosphere. We are particularly interested in the asymmetric structure of the vertical velocity field, assuming that the vertical velocity mainly determines the upper tropospheric WV in tropics. We use the linear shallow water equation on the equatorial $\beta-$plane as a conceptual tool to elucidate the dynamics which give rise to the Black Holes of upper tropospheric WV. We describe the asymmetries in the Hadley circulation and the Walker circulation. Then, we apply the linear theory with somewhat realistic heating and dissipation rates to the tropical circulation forced by ITCZ-type heating.

# 2 Method

## 2.1 The Linearized Equatorial $\beta$-Plane

Eigenvalue problem of the equatorial $\beta$-plane is first formulated and solved by *Matsuno* [5]. Heat-induced, frictionally controlled tropical circulation is studied by *Gill* [4] and others. Similar problem is solved by *Dias et al* [1] in the framework of stratified linear equatorial $\beta$-plane.

In this study, we use the equatorial $\beta$-plane, linear shallow water model similar to the model of *Gill* [4] as a conceptual tool to understand the governing dynamics. We calculate steady state solutions for the linear primitive equations forced by localized convection and dissipated by linear friction and radiative cooling.

The shallow water system can be considered as the representation of a vertical normal-mode in the stratified primitive equation [*Fulton [2]*]. For simplicity, we assume that the convective heating projects onto the first baroclinic mode only. Furthermore, we linearize the governing equation around the resting basic state. The model is now a single set of linear shallow water equations on the equatorial $\beta$-plane.

$$\frac{\partial u}{\partial t} - \beta y v + g\frac{\partial h}{\partial x} = -\epsilon_u u \tag{1}$$

$$\frac{\partial v}{\partial t} + \beta y u + g\frac{\partial h}{\partial y} = -\epsilon_v v \tag{2}$$

$$\frac{\partial h}{\partial t} + \bar{h}\left(\frac{\partial u}{\partial x} + \frac{\partial v}{\partial y}\right) = -\epsilon_h h - S, \tag{3}$$

where $u$ and $v$ are velocity components in the $x$- and $y$-directions, respectively, $h$ is the deviation of the fluid depth from the constant mean depth $\bar{h}$. Considering the vertical transform [*Fulton [2]*], the mean depth is given as the equivalent depth for the first baroclinic mode which is $570[m]$. $\beta y$ is the Coriolis parameter, $\epsilon_u$ is the constant for Rayleigh friction, and $\epsilon_h$ is the coefficient for Newtonian cooling. We parameterize the deep convection as a mass sink, $S(x, y, t)$.

Before solving (1)–(3) it is convenient to put the problem in nondimensional form. We define $c = (g\bar{h})^{\frac{1}{2}}$ as the constant gravity wave speed based on the mean depth $\bar{h}$. As

a horizontal length scale, let us choose the equatorial deformation radius, $L = (c/\beta)^{\frac{1}{2}}$. Similarly, a unit of time is determined as the time it takes for surface gravity wave to travel a unit of deformation radius, $T = (\beta c)^{-\frac{1}{2}}$. Data from the ITCZ in the Pacific (over the Marshall Islands) and in the Atlantic suggest that, for the first baroclinic mode, $c \approx 7.5 \times 10^1\, m/s$ and $\bar{h} \approx 5.7 \times 10^2\, m$, so that $L \approx 1.8 \times 10^3 km$ and $T \approx 0.28\, day$ [2]. We choose $\bar{h}$ as the unit of depth, so that (1)–(3) reduce to the nondimensional form

$$\frac{\partial u}{\partial t} - yv + \frac{\partial h}{\partial x} = -\epsilon_u u \tag{4}$$

$$\frac{\partial v}{\partial t} + yu + \frac{\partial h}{\partial y} = -\epsilon_v v \tag{5}$$

$$\frac{\partial h}{\partial t} + \frac{\partial u}{\partial x} + \frac{\partial v}{\partial y} = -\epsilon_h h - S \tag{6}$$

where all the independent variables $x$, $y$, $t$, all the dependent variables $u$, $v$, $h$, the parameter $\epsilon$ and the function $S(x, y, t)$ are now nondimensional. In the simple case where $\epsilon_u = \epsilon_h = \epsilon$, the system (4)–(6) can also be written in the more compact form

$$\frac{\partial \mathbf{w}}{\partial t} + \mathcal{L}\mathbf{w} = -\epsilon \mathbf{w} - \mathbf{S}, \tag{7}$$

where

$$\mathbf{w}(x,y,t) = \begin{pmatrix} u(x,y,t) \\ v(x,y,t) \\ h(x,y,t) \end{pmatrix}, \quad \mathbf{S}(x,y,t) = \begin{pmatrix} 0 \\ 0 \\ S(x,y,t) \end{pmatrix}, \quad \mathcal{L} = \begin{pmatrix} 0 & -y & \partial/\partial x \\ y & 0 & \partial/\partial y \\ \partial/\partial x & \partial/\partial y & 0 \end{pmatrix}. \tag{8}$$

## 2.2 Normal Mode Transformation

We solve the model equation (7) using the method of normal mode decomposition. We transform the model in spectral space in x. Defining $\hat{\mathbf{w}}(k, y, t)$ as the Fourier Transform of $\mathbf{w}(x, y, t)$, we can write the Fourier transform pair as

$$\hat{\mathbf{w}}(k,y,t) = \frac{1}{\sqrt{2\pi}} \int_{-\infty}^{\infty} \mathbf{w}(x,y,t) e^{-ikx}\, dx \tag{9}$$

$$\mathbf{w}(x,y,t) = \frac{1}{\sqrt{2\pi}} \int_{-\infty}^{\infty} \hat{\mathbf{w}}(k,y,t) e^{ikx}\, dk \tag{10}$$

We define the linear operator $\hat{\mathcal{L}}$ identical to $\mathcal{L}$ but with $\frac{\partial}{\partial x}$ replaced by $ik$.

$$\hat{\mathcal{L}} = \begin{pmatrix} 0 & -y & ik \\ y & 0 & d/dy \\ ik & d/dy & 0 \end{pmatrix}. \tag{11}$$

We also define the inner product,

$$(\mathbf{f},\mathbf{g}) = \int_{-\infty}^{\infty} (f_1 g_1^* + f_2 g_2^* + f_3 g_3^*) dy, \tag{12}$$

given

$$\mathbf{f} = \begin{pmatrix} f_1 \\ f_2 \\ f_3 \end{pmatrix}, \qquad \mathbf{g} = \begin{pmatrix} g_1 \\ g_2 \\ g_3 \end{pmatrix}, \tag{13}$$

where we use the $^*$ symbol to denote the complex conjugate.

The adjoint of $\hat{\mathcal{L}}$ with respect to the inner product (12) is an operator $\hat{\mathcal{L}}^\dagger$ which satisfies

$$(\hat{\mathcal{L}}\mathbf{f},\mathbf{g}) = (\mathbf{f},\hat{\mathcal{L}}^\dagger\mathbf{g}) \tag{14}$$

for all $\mathbf{f}(y)$ and $\mathbf{g}(y)$ satisfying the boundary conditions. Dias et al. [1] shows that the operator $\hat{\mathcal{L}}$ is skew-Hermitian (i.e., $\hat{\mathcal{L}}^\dagger = -\hat{\mathcal{L}}$) so that (14) becomes

$$(\hat{\mathcal{L}}\mathbf{f},\mathbf{g}) = -(\mathbf{f},\hat{\mathcal{L}}\mathbf{g}). \tag{15}$$

The eigenvalues of $\hat{\mathcal{L}}$ are purely imaginary, and the eigenfunction form an orthogonal set. Let us define the eigenvalue $i\omega$ and the eigenfunction $\mathbf{K}$. They satisfies following relationship.

$$\hat{\mathcal{L}}\hat{\mathbf{K}} = i\omega\hat{\mathbf{K}}, \tag{16}$$

The solutions to (16) are discussed in detail by *Matsuno* [5]. We summarize the relevant results here.

Equation (16) has bounded solutions, as $y \to \pm\infty$, only if $\omega^2 - k^2 - k/\omega$ is an odd integer. It results in the cubic dispersion relationship.

$$\omega^2 - k^2 - \frac{k}{\omega} = 2n + 1 \tag{17}$$

with $n = 0, 1, 2, \ldots$ for $\omega$ has three roots for given $k$ and $n$. We denote the solutions of this cubic equation by $\omega_{n,r}(k)$ to indicate which of the three roots of the frequency equation we are discussing. The subscript $r$ ($r = 0, 1, 2$) is related to Rossby modes ($r = 0$), Westward-propagating Inertial Gravity modes ($r = 1$), and Eastward-propagating Inertial Gravity modes ($r = 2$). Let $\mathbf{K_{n,r}}$ denote the eigenfunction corresponding to $r$th root of (17) given $n$.

$$\mathbf{K}(k,y) = \begin{pmatrix} \mathcal{U}(k,y) \\ \mathcal{V}(k,y) \\ \mathcal{H}(k,y) \end{pmatrix} \tag{18}$$

$$= A_{n,r} e^{-\frac{1}{2}y^2} \begin{pmatrix} -\frac{1}{2}(\omega_{n,r}+k)H_{n+1}(y) - n(\omega_{n,r}-k)H_{n-1}(y) \\ i(\omega_{n,r}^2 - k^2)H_n(y) \\ -\frac{1}{2}(\omega_{n,r}+k)H_{n+1}(y) + n(\omega_{n,r}-k)H_{n-1}(y) \end{pmatrix} \tag{19}$$

where

$$A_{n,r} = \pi^{-\frac{1}{4}}\{2^n n![(n+1)(\omega_{n,r}+k)^2 + n(\omega_{n,r}-k)^2 + (\omega_{n,r}^2 - k^2)^2]\}^{-\frac{1}{2}} \tag{20}$$

is a normalization constant which assures that

$$(\mathbf{K_{n,r}}, \mathbf{K_{n,r}}) = 1 \tag{21}$$

The Hermite polynomials $H_n(y)$ are given by $H_0(y) = 1$, $H_1(y) = 2y$, $H_2(y) = 4y^2 - 2$, $H_3(y) = 8y^3 - 12y$, $\cdots$, with recurrence relation $H_{n+1}(y) = 2yH_n(y) - 2nH_{n-1}(y)$.

Special care must be taken when $n = 0$, in which case the dispersion relation factors to $(\omega_{0,r} + k)(\omega_{0,r}^2 - k\omega_{0,r} - 1) = 0$. The root $\omega_{0,r} = -k$ must be discarded because the corresponding eigenfunction cannot be determined. Thus, for $n = 0$, only the two roots of $\omega_{0,r}^2 - k\omega_{0,r} - 1 = 0$ are allowed.

In addition, we obtain Kelvin mode by setting $\hat{v} = 0$. The eigenvalue for Kelvin mode is $\omega_{-1} = \pm k$. The subscript $-1$ is chosen because the dispersion relation $\omega = k$ is a solution of $\omega^2 - k^2 - k/\omega = 2n + 1$ when $n = -1$. The eigenfunction is

$$\mathbf{K_{-1}} = A_{-1}e^{-\frac{1}{2}y^2}\begin{pmatrix}1\\0\\1\end{pmatrix}, \tag{22}$$

with corresponding eigenvalue $\omega_{-1} = k$.

Since $\hat{\mathbf{K}}_{n,r}$ is orthogonal and complete, and we can introduce the meridional transform pair using the normal modes.

$$\hat{w}_{n,r}(k,t) = (\hat{\mathbf{w}}(k,y,t), \mathbf{K}_{n,r}(k,y)) \tag{23}$$

$$\hat{\mathbf{w}}(k,y,t) = \sum_{r=0}^{2}\sum_{n}^{\infty}\hat{w}_{n,r}(k,t)\mathbf{K}_{n,r}(k,y) \tag{24}$$

We may now use our eigenfunction to decompose the time dependent problem into normal modes.

Taking the inner product of the Fourier transform of (7) with $\mathbf{K}_{n,r}(k,y)$, we obtain

$$\left(\frac{\partial\hat{\mathbf{w}}(k,y,t)}{\partial t}, \mathbf{K}_{n,r}(k,y)\right) + \left(\hat{\mathcal{L}}\hat{\mathbf{w}}(k,y,t), \mathbf{K}_{n,r}(k,y)\right) =$$

$$-\epsilon\left(\hat{\mathbf{w}}(k,y,t), \mathbf{K}_{n,r}(k,y)\right) - \left(\hat{\mathbf{S}}(k,y,t), \mathbf{K}_{n,r}(k,y)\right)$$

$$\frac{d\hat{w}_{n,r}(k,t)}{dt} + (\epsilon + i\omega_{n,r})\hat{w}_{n,r}(k,t) = -\hat{S}_{n,r}(k,t)$$

Equation (25) is the transformation to spectral space of the original system (7) and has steady solution

$$\overline{\hat{w}_{n,r}}(k,t) = -\frac{\hat{S}_{n,r}(k)}{\epsilon + i\omega_{n,r}}. \tag{25}$$

When this is inserted into (24), we obtain the steady solution in spectral space

$$\overline{\hat{\mathbf{w}}}(k,y,t) = \sum_{n,r} \overline{\hat{w}_{n,r}}(k)\mathbf{K}_{n,r}(k,y) \tag{26}$$

Taking the inverse Fourier transform of (26) and breaking back into component form, we obtain our final physical space solution.

$$\overline{\mathbf{w}}(x,y,t) \;=\; (2\pi)^{-\frac{1}{2}} \int_{-\infty}^{\infty} \overline{\hat{\mathbf{w}}}(k,y,t)e^{ikx}\,dk \tag{27}$$

The solution of our initial value problem consists of a superposition of normal modes. The superposition involves all zonal wavenumbers (integral over $k$), all meridional normal modes (sum over $n$ and $r$). It should be noted that typical superpositions of many normal modes result in spatial patterns which differ greatly from individual normal modes.

### 2.3 Forcing

The dynamical role of the deep convection, in general, can be described as a mass sink in the lower atmosphere and as a source in the upper atmosphere. We parameterize the deep convection (ITCZ) as a mass sink whose shape is gaussian in $x$ and $y$, assuming that our model represents the lower troposphere.

$$S(x,y) = S_o e^{-x^2/a^2} e^{-(y-y_0)^2/b^2} \tag{28}$$

where $y_0$ is the center of the Gaussian shaped mass sink, $a$ is its $e$-folding width in $x$, and $b$ its $e$-folding width in $y$. The factor, $S_o[m/s]$, is the maximum rate of the mass removal and represents the intensity of the deep convection. Realistic measure of $S_o[m/s]$ could be obtained as the projection of the diabatic heating onto the first baroclinic mode.

The Fourier transform of this forcing is

$$\hat{S}(k,y) = 2^{-\frac{1}{2}} S_o a e^{-(y-y_0)^2/b^2} e^{-\frac{1}{4}k^2a^2} \tag{29}$$

Then, using (23), we obtain

$$\begin{aligned}
\hat{S}_{n,r}(k,t) \;&=\; \left(\hat{\mathbf{S}}(k,y), \mathbf{K}_{n,r}(k,y)\right) = \int_{-\infty}^{\infty} \hat{S}(k,y,t)\mathcal{H}_{n,r}(k,y)dy \\
&=\; S_o\sqrt{\pi}abA_{n,r}(2+b^2)^{-\frac{1}{2}} e^{-\frac{1}{4}k^2a^2} e^{-y_0^2/(2+b^2)}. \\
&\left\{ -\tfrac{1}{2}(\omega_{n,r}+k)\left(\frac{2-b^2}{2+b^2}\right)^{\frac{n+1}{2}} H_{n+1}\left(\frac{2y_0}{(4-b^4)^{\frac{1}{2}}}\right) + n(\omega_{n,r}-k)\left(\frac{2-b^2}{2+b^2}\right)^{\frac{n-1}{2}} H_{n-1}\left(\frac{2y_0}{(4-b^4)^{\frac{1}{2}}}\right)\right\}
\end{aligned}$$

for $0 < b < 2^{\frac{1}{2}}$ and $n \geq 0$. For the Kelvin mode, $\hat{S}_{-1,2}(k,t)$ can be written as

$$\hat{S}_{-1,2}(k,t) = \frac{A_{-1,2}}{\sqrt{\pi(b^2+2)}} exp\{-(\frac{k^2a^2}{4} + \frac{y_o^2}{b^2+2})\} \tag{30}$$

## 2.4 Dissipation

The time scales for the kinetic energy dissipation and the radiative cooling are different. We expand the theory such that the dissipation rate can be different between $u$, $v$, and $h$. The time dependent equation becomes

$$\frac{\partial \hat{\mathbf{w}}}{\partial t} + \hat{\mathcal{L}}\hat{\mathbf{w}} = -\epsilon_u(\mathbf{I} - \mathbf{F})\hat{\mathbf{w}} - \hat{\mathbf{S}} \tag{31}$$

where $\mathbf{I}$ is the identity matrix and

$$\mathbf{F} \equiv \begin{pmatrix} 0 & 0 & 0 \\ 0 & 0 & 0 \\ 0 & 0 & 1 - \frac{\epsilon_h}{\epsilon_u} \end{pmatrix} \tag{32}$$

We substitute $\hat{\mathbf{w}}$ with $\sum_{n',r'} \hat{w}_{n',r'}(k)\mathbf{K}_{n',r'}(k,y)$ and take the inner product with $\mathbf{K}_{n,r}(k,y)$. We obtain

$$\frac{d\hat{w}_{n,r}(k,t)}{dt} + (\epsilon + i\omega_{n,r})\hat{w}_{n,r}(k,t) = -\hat{S}_{n,r}(k,t) + \epsilon_u \sum_{n',r'} \hat{w}_{n',r'} \left(\mathbf{F}\mathbf{K}_{n',r'}, \mathbf{K}_{n,r}\right) \tag{33}$$

Applying the relationship (32),

$$\frac{d\hat{w}_{n,r}(k,t)}{dt} + (\epsilon + i\omega_{n,r})\hat{w}_{n,r}(k,t) = -\hat{S}_{n,r}(k,t) + (\epsilon_u - \epsilon_h) \int_{-\infty}^{\infty} \sum_{n',r'} \hat{w}_{n',r'} \mathcal{H}_{n',r'} \mathcal{H}^*_{n,r}\, dy \tag{34}$$

when $(\epsilon_u - \epsilon_h) \ll 1$, the steady state solution is to a good approximation

$$\hat{w}_{n,r} = \hat{w}^{(0)}_{n,r} + \hat{w}^{(1)}_{n,r}(\epsilon_u - \epsilon_h) + \hat{w}^{(2)}_{n,r}(\epsilon_u - \epsilon_h)^2 + \ldots \tag{35}$$

where

$$\hat{w}^{(0)}_{n,r} = -\frac{\hat{S}_{n,r}(k)}{\epsilon_u + i\omega_{n,r}} \tag{36}$$

$$\hat{w}^{(m+1)}_{n,r} = \frac{1}{\epsilon_u + i\omega_{n,r}} \int_{-\infty}^{\infty} \sum_{n',r'} \hat{w}^{(m)}_{n',r'} \mathcal{H}_{n',r'} \mathcal{H}^*_{n,r}\, dy \tag{37}$$

for $m = 0, 1, 2, \ldots$. Thus, the normal modes are coupled in the time dependent equation when the time scale for kinetic energy dissipation and radiative cooling are different. For the special case, $(\epsilon_u = \epsilon_h)$, it is identical to (25).

# 3 Simple Cases

## 3.1 Steady Solution to an Idealized Forcing

Equation (26) shows that the model solution is expressed as the infinite sum of the normal modes to represent the full solution. We turncate the solution at $n = 200$ including the first 200 normal modes for the Rossby, Kelvin, and inertial gravity modes. This introduces an error in the final solution. The power spectrum of $\hat{S}_{n,r}$ suggests that including 200 normal modes with reduce the error less than 0.01 %.

We first describe the steady state solution for $u$, $v$, $h$, and $w$ to illustrate the response to the forcing. As a simple representation of ITCZ, we use non-dimensional length scales $a = 1.5$, $b = 0.25$, and $y_o = 0.7$ which are equivalent of $a = 2700[km]$, $b = 450[km]$, and $y_o = 1260[km]$. For dissipation rates, we chose nondimensional parameter $\epsilon_u = 0.1$ and $\epsilon_h = 0.03$ which are equivalent of $\epsilon_u = 0.36[day^{-1}]$ and $\epsilon_h = 0.11[day^{-1}]$. $S_o$ is taken to be $57[m \cdot day^{-1}]$ using the Marshall Island data [2].

Figure 2 shows the steady state solution for $u$, $v$, $h$, and $w$ for this forcing. The geopotential height perturbation has its minimum near the location of the deep convection associated with the cycloninc circulation. The circulation tends to converge near the forcing, and produces intensified upward motion on the order of $50[m/day]$. Outside of the rising region, we have a region of the mild sinking which has two peaks in the north-west of the forcing and the directly south of the forcing. Spatial structure of the sinking motion can be understood as the superposition of the responses from different normal modes.

## 3.2 Decomposition into Normal Modes

Since the full solution is the sum of all the normal modes, one can take a partial sum to find contributions from individual mode. Throughout this study, the eigenfunctions of the inviscid, free solution are used as the orthonormal basis for the normal mode transformation. These basis are not the eigenfunction of the frictionally-controlled, heat-induced problem. However, the decomposition of the full solution into the "inviscid modes" gives insights into the spatial structure of the solution.

Figure 3 shows the decomposition of the sinking motion into four normal modes; Rossby modes, westward-propagating inertial gravity modes, eastward-propagating inertial gravity modes, and the Kelvin mode. The Rossby modes, the inertial gravity modes, and the Kelvin mode have distinct spatial structure in the vertical motion.

In general, sinking motions associated with the Rossby modes are located at the west of the forcing because Rossby waves propagates to the west. The response of the mixed mode is responsible for the strong sinking motion asymmetric across the equator. The mixed mode is excited when the forcing is asymmetric about the equator.

The sinking motion associated with the inertial gravity modes have two peaks; one to the north, and another to the south of the forcing. The eastward-propagating inertial gravity modes have stronger sinking motion to the south of the forcing. This strong sinking at the south of the forcing is associated with the mixed mode.

The Kelvin mode is always symmetric about the equator and its sinking motion is always located to the east of the forcing because the Kelvin waves propagates to the east.

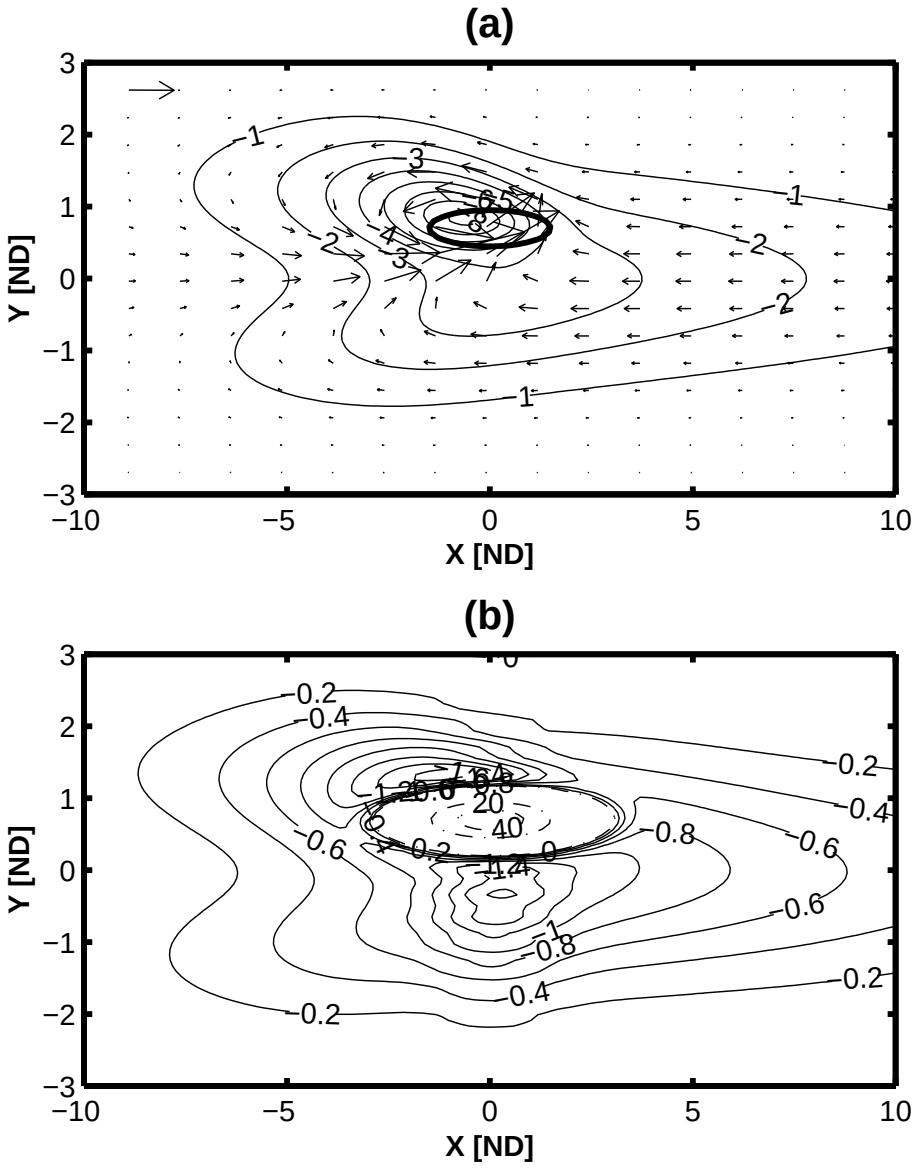


Figure 2: **Steady state solution for $u$, $v$, $h$, and $w$. (a):** The height perturbation and the wind field. The contour interval is $1[m]$ for height. For the wind field, the reference vector ($1[m/s]$) is drawn at the upper left corner of the domain. **(b):** Vertical motion. The solid contour is sinking motion with the contour interval of $0.2[m/day]$. The dash-dotted lines are rising motion with the contour interval of $20[m/day]$

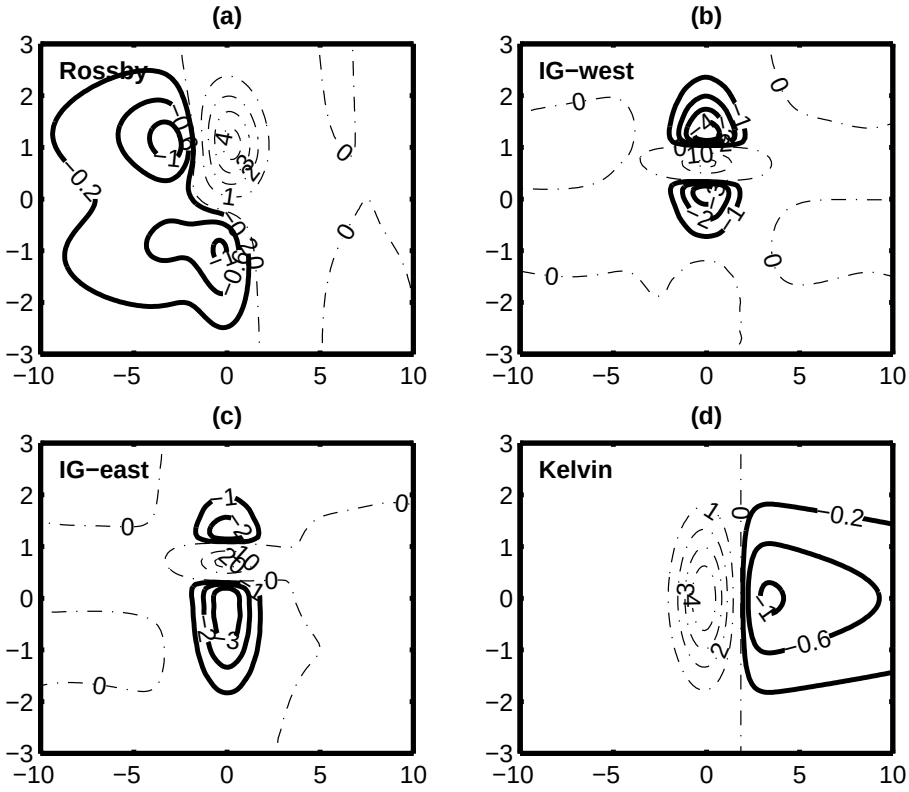


Figure 3: **Decomposition of $w$ into normal modes.** The vertical motion, $w$, is decomposed into normal modes of four categories. Solid line represents the contour of the sinking motion, and the dash-dotted line represents the contour of the rising motion. **(a):** Rossby modes ($r = 0, n = 0, 1, 2, \ldots$), **(b):** Westward-propagating inertial gravity modes ($r = 1, n = 1, 2, \ldots$), **(c):** Eastward-propagating inertial gravity modes ($r = 2, n = 0, 1, 2, \ldots$), **(d):** Kelvin mode ($r = 2, n = -1$). For the Rossby modes and the Kelvin mode, contour interval for sinking motion is $0.4[m/day]$, and the contour interval for the rising motion is 1 [m/day]. For the inertial gravity modes, contour interval for sinking motion is $1[m/day]$, and the contour interval for the rising motion is 10 [m/day].

The maximum amplitude of the vertical motion of the inertial gravity modes is much stronger and more localized than that of the Rossby modes and the Kelvin mode. Although the Rossby modes and the Kelvin mode are less intense, they have much greater spatial extent. When these four vertical motions are added together, it becomes identical to the total solution shown in Figure 2.

The asymmetric structure of the sinking motion can be understood as following. The east-west asymmetry of the vertical motion is greatly affected by the competition between the Rossby modes and the Kelvin mode. This corresponds to what we call "the Walker Circulation". On the other hand, the north-south asymmetry of the vertical motion is related to the inertial gravity modes. This corresponds to what we call "the Hadley Circulation". To illustrate these idea, we examine the zonally averaged circulation and meridionally averaged circulation.

### 3.3 Hadley Circulation

Spatially averaged circulation can be s simple indicator for the asymmetric structure of the vertical motion. Figure 4 is the zonally averaged stream function (a) and meridional velocity in the lower troposphere (b). There is a rising motion at the location of the deep convection. The winter branch of the Hadley circulation is much stronger than the summer branch. The sinking motion is wide and intense in the winter hemisphere. This asymmetry in the Hadley circulation can be explained in several ways.

First, Coriolis parameter (equivalent of the inertial stability in the equatorial $\beta$-plane) is very small in the vicinity of the equator. The small Coriolis parameter suggests that the deformation radius, $\sqrt{g\overline{h}}/f$, is greater near the equator. Therefore, the spatial scale of the circulation must be greater in the winter hemisphere.

Secondly, the zonally averaged velocities on the equator at steady state is given by

$$\overline{u}^x = 0 \tag{38}$$

$$\overline{v}^x = -\frac{g}{\epsilon_v}\frac{\partial \overline{h}^x}{\partial y} \tag{39}$$

It suggests no zonal flow nearby the equator. Since the convective forcing produces strong meridional gradient of $\overline{h}^x$, the winter branch of the Hadley circulation is enhanced.

Finally, the zonally-averaged meridional velocity, $\overline{v}^x$, is decomposed into normal modes in Figure 4 (b). There is no contribution from Kelvin mode since $v = 0$ always in Kelvin mode. The spatial structure of $\overline{v}^x$ is governed by inertial gravity modes. The contribution from Rossby modes are dominated by the mixed Rossby-gravity mode. The eastward-propagating inertial gravity modes has the strongest intensity in the winter hemisphere because it has contribution from the mixed Rossby-gravity mode as well. The convective forcing which is asymmetric about the equator excites the mixed Rossby-gravity mode and it produces large fraction of the cross-equatorial transport in the zonally averaged circulation.

The north-south asymmetry of the vertical motion is associated with the mixed Rossby-gravity mode, and it has intensified sinking in the winter hemisphere. This is consistent with the satellite image in Figure 1.

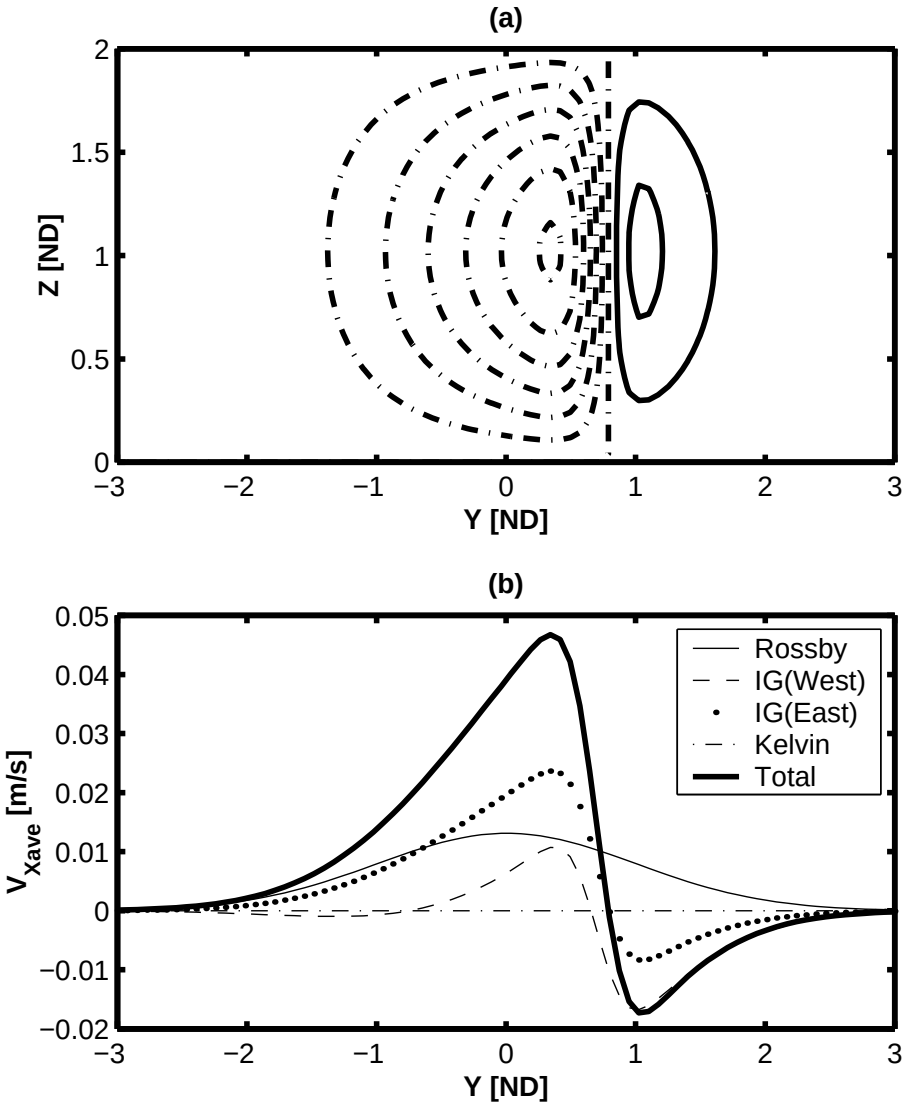


Figure 4: **Hadley Circulation** (a) The meridional stream function. (b) The zonally averaged meridional velocity in the lower layer. The zonal average is first calculated using spectral method. The vertical structure is assumed to be the first baroclinic mode.

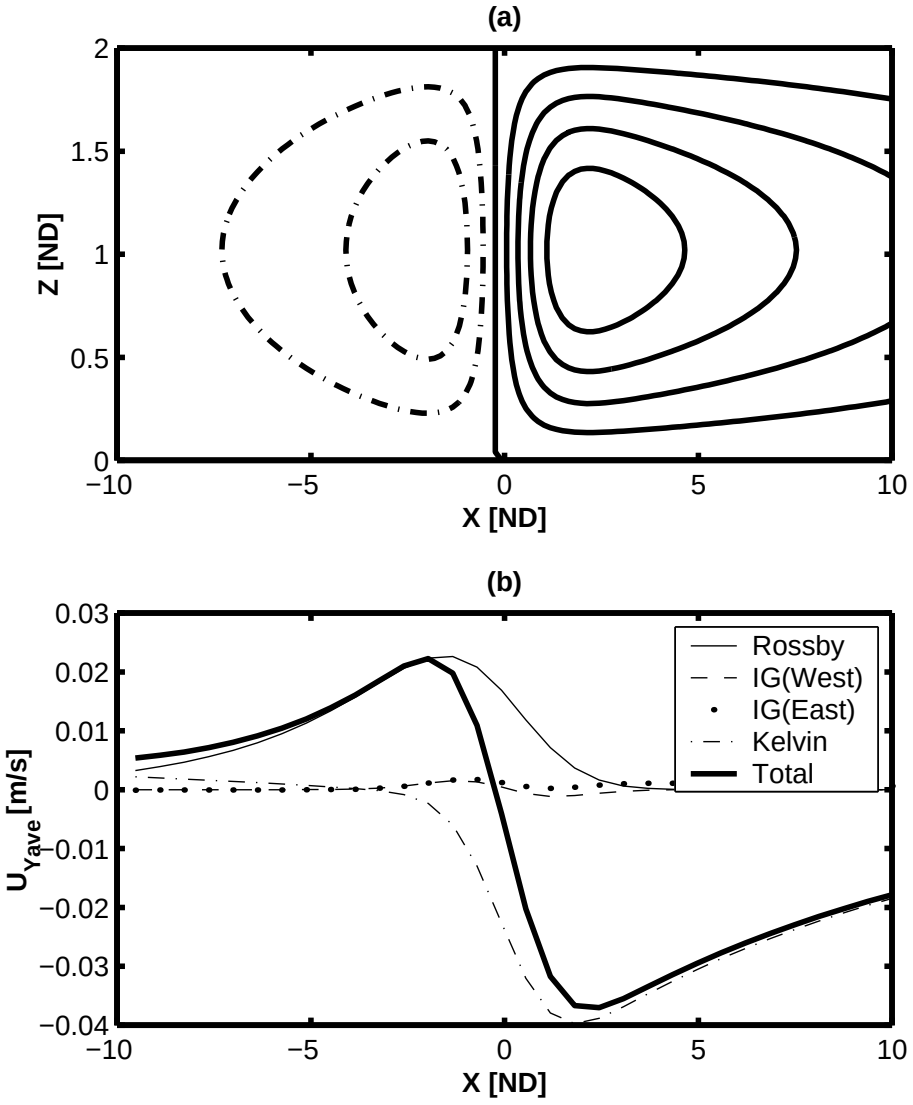


Figure 5: **Walker Circulation** (a) Zonal stream function. (b) Meridionally averaged zonal velocity in the lower layer. The vertical structure for the stream function is given by the first baroclinic mode.

### 3.4 Walker Circulation

Figure 5 is the meridionally averaged stream function (a) and zonal velocity in the lower troposphere (b). It shows the east-west asymmetry of the Walker circulation. There is a rising motion near the location of the deep convection. The eastern branch of the Walker circulation is stronger than the western branch in this particular example. This asymmetry in the Walker circulation can be explained as the competition between Kelvin mode and Rossby modes.

Figure 5 (b) suggests that the eastern branch is dominated by the Kelvin mode and the western branch is dominated by the Rossby modes. This result is robust with wide range of parameters. It implies that the east-west asymmetry of the Walker circulation reflects the relative intensity of the Rossby modes and the Kelvin mode and its dependence on model parameters.

First, let us consider the Kelvin mode. The projection of the Gaussian-type heating onto the Kelvin mode is shown in Equation (30). It suggests that the forcing has structure such that the intensity of the Kelvin mode decays with $y_o$. Physically, it means that the forcing projects less onto the Kelvin mode when there is a greater distance between the center of the forcing and the equator because the Kelvin mode is trapped nearby the equator. The eastern branch of the Walker circulation weakens with increasing $y_o$ while $a$ and $b$ are fixed.

Secondly, let us consider the Rossby modes. The response of the Rossby modes to varying $y_o$ is illustrated by considering the potential vorticity equation of the system. The potential vorticity equation can be constructed from Equation (4), (5) and (6).

$$\frac{\partial q}{\partial t} + v = -\epsilon q + yS \tag{40}$$

where $q \equiv \frac{\partial v}{\partial x} - \frac{\partial u}{\partial y} - yh$ is the perturbation potential vorticity in the shallow water system. This PV perturbation is mostly associated with the Rossby modes. It is remarkable that the forcing term in the PV equation (40) is proportional to $y$. This is due to the increase in the Coriolis term with $y$. Therefore, the Rossby modes intensifies with increasing $y_o$. Here, the sensitivity of the Rossby modes has opposite sign from that of the Kelvin mode.

Figure 6 shows the sensitivity of the stream functions to the center of the heating, $y_o$. Figure 6 (a) clearly shows that the eastern branch weakens and the western branch intensifies as $y_o$ increases. The western branch becomes stronger than the eastern branch when $y_o \sim 1.1$ or greater. Figure 6 (b) confirms the view that the winter hemisphere has stronger sinking motion, and the north-south asymmetry grows with increasing $y_o$.

## 4 Somewhat Realistic Solution

The satellite image (e.g. Figure 1) shows quite complicated WV distribution and the time series of the satellite image suggests that it is quite variable. Here, we try to reproduce the large-scale pattern of the dry region in the upper troposphere using the simple model we derived and studied in the previous section. As a first attempt, we study the steady state response of the shallow water system to the multiple convective region. Since the model is linear, the circulation due to the multiple heating can be obtained as the superposition of the circulations due to individual forcing.

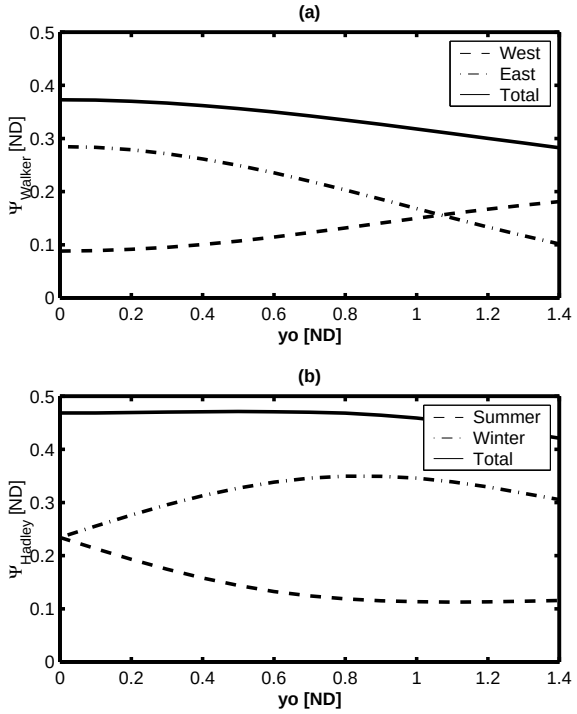


Figure 6: **The sensitivity of the maximum mass transport to the location of the forcing, $y_o$.** (a) The intensity of the Walker circulation and contributions from its eastern branch and the western branch. (b) The intensity of the Hadley circulation and contributions from its northern branch and the southern branch. The intensity is measured as the maximum value of the stream function.

Table 1: **The size and the location of the deep convection** In the case of the Eastern Pacific in the late July, 2001.

| Deep Convection Site | Location $(x_o, y_o)$ | Size $(a, b)$ |
|---|---|---|
| A : ITCZ | $(0, 0.7)$ | $(1.5, 0.25)$ |
| B : PNG | $(-5, 0)$ | $(0.5, 0.5)$ |
| C : SPCZ | $(-1, -1.5)$ | $(0.5, 0.5)$ |

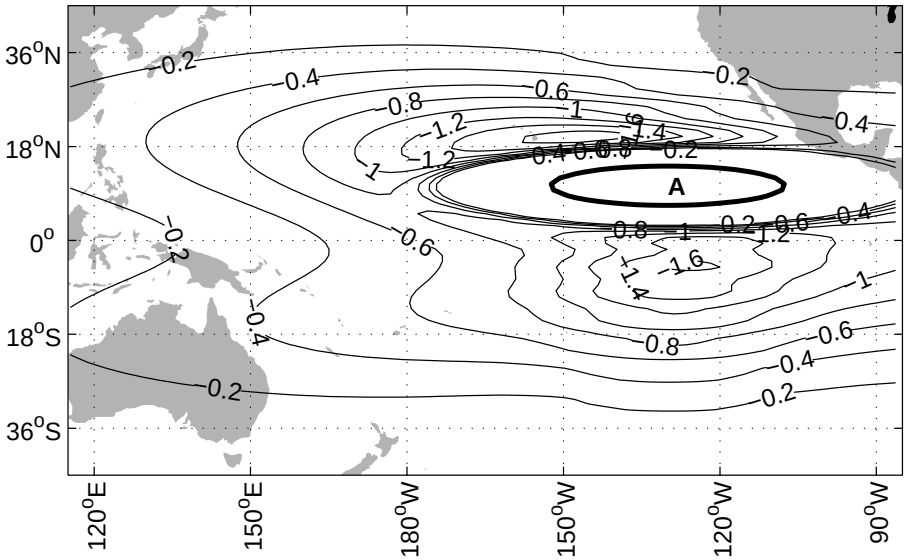


Figure 7: **Steady Solution for the sinking motion due to ITCZ over Eastern Pacific**

Considering the case in the Eastern Pacific in the late July in 2001, (shown in Figure 1), we seem to have two or three sites of convection and they are listed in the Table 4. **(A)**: ITCZ over tropical Pacific is the narrow band of the moist region in the satellite image. This feature is tied to the warm SST over the ocean and often appears around 10N over the Pacific ocean. **(B)**: The deep convection over Papua New Guinea (PNG) is located in the tropical Western Pacific. In the La Nina condition, there is a warm pool in the Western Pacific, and the deep convection is tied to the warm SST. **(C)**: The satellite image suggests that the moist region in the South Pacific which is often called "South Pacific Convergence Zone" (Hereafter, SPCZ). The WV image is more stable in time and space at the deep convection site over Eastern Pacific ITCZ or over PNG. SPCZ is highly variable due to the weather-type baroclinic waves.

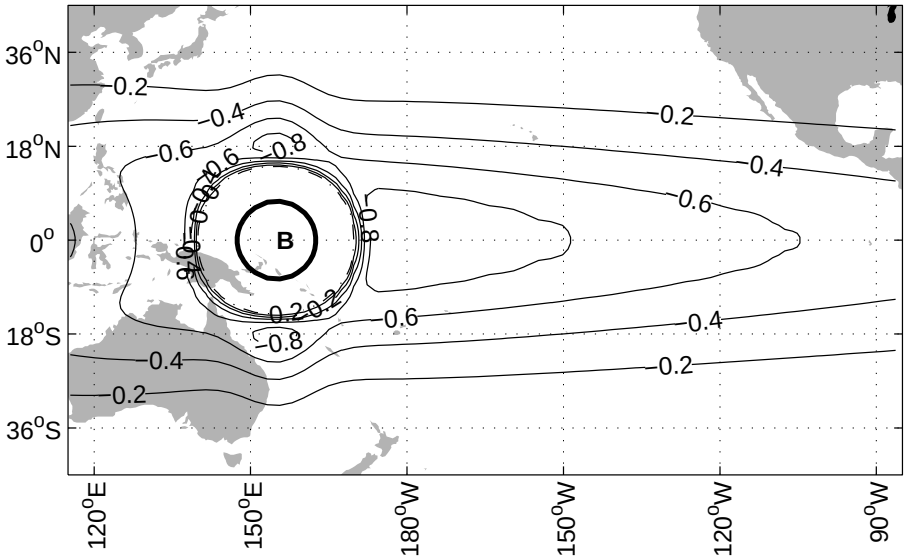


Figure 8: **Steady Solution for the sinking motion due to the deep convection over PNG**

## 4.1 (A) ITCZ over Eastern Pacific

Figure 7 shows the distribution of the sinking motion at steady state induced by the deep convection over the Eastern Pacific. The pattern suggests that there are two sinking motion maximum. An intense sinking region is located in the southern hemisphere approximately at the same latitude as the forcing (120°W, 8°S). This sinking motion is due to the inertial-gravity modes and the mixed mode. Another intense sinking region is located in the subtropical Eastern pacific around (145°W, 18°N). The spectral decomposition suggests that this is caused by the Rossby mode. The intensity of the latter one is weaker.

## 4.2 (B) The deep convection over PNG

Figure 8 shows the distribution of the sinking motion at steady state induced by the deep convection over PNG. The pattern suggests that there is a strong response to the east of the convective forcing caused by the Kelvin mode. The sinking motion is symmetric about the equator. There are secondary maximum directly north and south of the forcing induced by the inertial-gravity modes.

## 4.3 (C) The SPCZ forcing

Figure 9 shows the distribution of the sinking motion at steady state induced by SPCZ. The pattern suggests that there is almost no sinking motion to the east of the forcing. The response of the Kelvin mode is very weak because the forcing is located at greater distance from the equator. The response of the Rossby mode is very strong, creating an intense sinking motion to the west of the forcing. There is an intense response in the mixed mode, which causes the sinking motion in the northern hemisphere. The intensity of the sinking

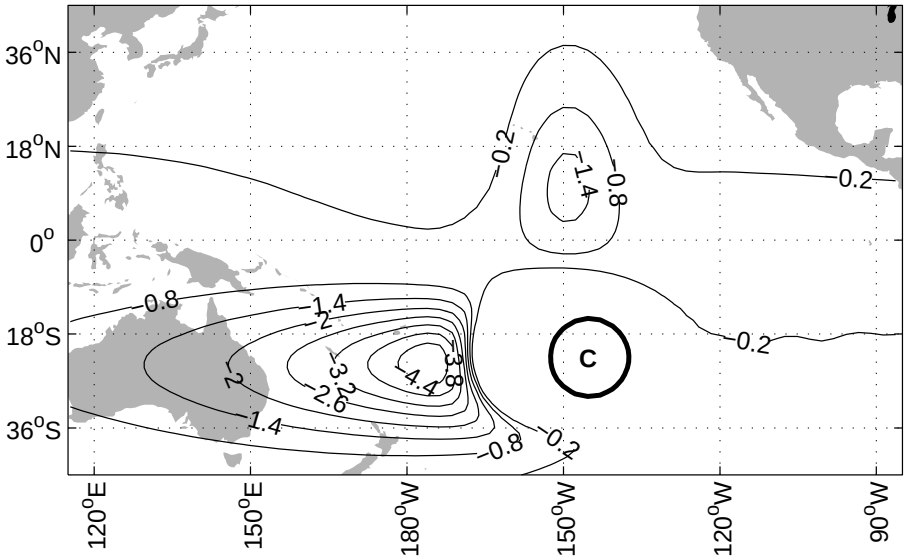


Figure 9: **Steady Solution for the sinking motion due to SPCZ**

motion is much stronger than (A) or (B) partly because of the magnitude of the forcing, S, is prescribed at the same value as (A) and (B). In reality, the magnitude of the convective forcing is much weaker in SPCZ than in ITCZ. Thus, we do not expect to observe this strong sinking motion in the satellite image.

### 4.4 Response to the multiple heating region

Here, we show the steady state response to the multiple convective region in Figure 10. Since the model is linear, the circulation due to the multiple heating can be obtained as the superposition of the responses to the individual forcing. The intensity of the convective forcing could be different between the forcing (A), (B), and (C). The resulting solution, however, has a robust spatial structure which does not depend of the choice of the relative importance of individual forcing. In Figure 10, the relative intensity of the forcing is prescribed to A:B:C=3:6:1.

The solution for the multiple convective region resembles the satellite image of the black hole of WV remarkably well. The simple model reproduces the intense sinking motion around (120°W, 8°S) which is a combination of the responses to the forcing (A) and (B). This intense sinking motion could explain the formation of the black hole in the winter hemisphere. SPCZ does not contribute to the sinking motion near the black hole.

The solution also agrees with the satellite observation that the relatively dry region in the subtropical Eastern Pacific around (150°W, 20°N).

## 5 Discussion

Let us summarize the main results.

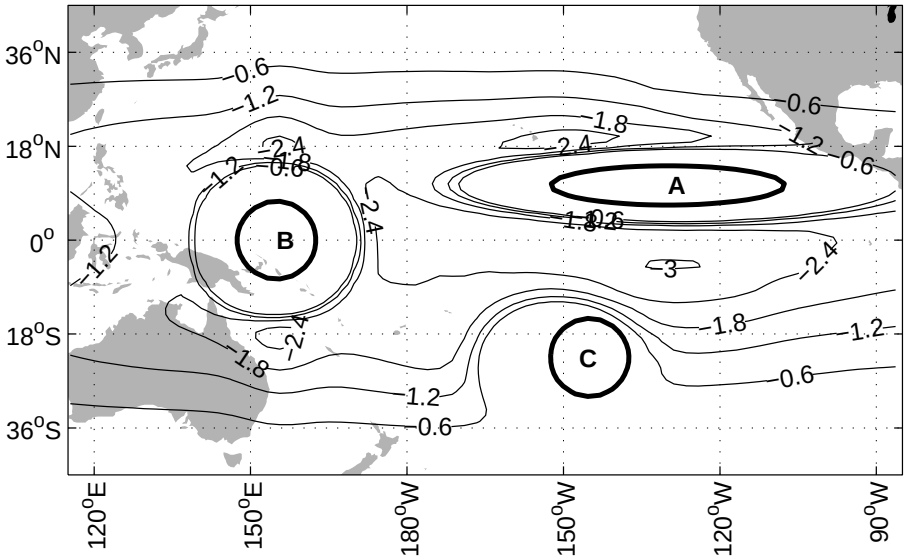


Figure 10: **Steady Solution for the multiple convective region**

- (1) The spectral decomposition into "inviscid normal modes" suggests that the Hadley circulation is mainly sustained by the inertial-gravity modes.
- (2) The asymmetry in the Walker circulation is driven by the competition between the Kelvin mode and the Rossby modes.
- (3) The solutions to the simple, linear shallow water model agrees with the the spatial structure of the upper tropospheric WV satellite images remarkably well.
- (4) The Black Hole of the WV in the tropical Pacific can be understood as the circulation induced by the deep convection over the central Pacific and over Papua New Guinea.

The result (3) and (4) are further tested against several variants of similar experiments with different relative intensity of the convective forcing. Those experiments confirmed that the spatial structure predicted by this simple model is a robust one. It is of interest to examine the sinking motion over the Atlantic ocean and the Indian ocean, which can test the validity of the simple linear theory.

This simple model seems to behave particularly well near the equator where the background flow is relatively weak. The linear assumption breaks down when there is a significant background flow because the model is linearized around the state of rest, which is not applicable in the middle latitudes. Near the location of the convective heating, the flow velocity is also large which causes the linearity to break down.

It can be shown that, in some parameter regime, the potential velocity distribution associated with the steady state solution is unstable to barotropic instability or baroclinic instability [*Gerber et al* [3]]. The dynamical instabilities causes the formation of eddies and the break up of ITCZ. This is also the limitation of the theory based upon the steady state.

Despite the simplicity of the model, this study shows that the linear shallow water model can be used as a conceptual tool for understanding and explaining the upper tropospheric water vapor. It motivates the further investigation of the simple model with emergent questions on the upper tropospheric water vapor. *Rosendal* [8] pointed out the statistical relationship between black holes of water vapor appearing in the winter hemisphere and the development of tropical cyclones in the summer hemisphere.

## 6 Acknowledgment

The authors are thankful to Joe Keller and Bill Young for helpful comments and discussion. TI is also thankful to Mitsuko Ito, Janet Fields, and all the GFD 2001 fellows for continuous encouragement and support.

## References

[1] Dias, P. L. S., W. H. Schubert, and M. DeMaria, "Large-Scale Response of the Tropical Atmosphere to Transient Convection" J. Atmos. Sci. Quart. **40**, 2689 (1983).

[2] Fulton S. and W.H. Schubert, "Vertical Normal Mode Transforms: Theory and Application", Monthly Weather Review, **113**, 647, (1985)

[3] Gerber E.P., T. Ito, and W.H. Schubert, "The Time Evolution of Arid, Black Holes in Upper Tropospheric Water Vapor", in *GFD-2001 volume*, (Woods Hole Oceanographic Institution), (2001)

[4] Gill, A. E., "Some simple solutions for heat induced tropical circulation" Quart. J. Roy. Meteorol. Soc. **106**, 447 (1980).

[5] T. Matsuno, "Quasi-Geostrophic Motions in the Equatorial Area", J. Meteorol. Soc. Japan, **44** 25 (1966).

[6] J. Pedlosky, *Geophysical Fluid Dynamics*, 2nd ed. (Springer Verlag, New York, 1987).

[7] Picon L. and M. Desbios, Relation between METEOSAT Water Vapor Radiance Fields and Large Scale Tropical Circulation Features, Journal of Climate, **3**, 865, (1990)

[8] Rosendal H., "The Black Hole of Water Vapor and Its Use as an Indicator of Tropical Cyclone Development and Intensity Changes", http://members.aol.com/Rosendalhe/black.htm, (1998)

[9] Schmez J. et al., "Monthly Mean Large Scale Analysis of Upper Tropospheric Humidity and Wind Field Divergence Derived from Three Geostationary Satellites" Bulletin of American Meteorological Society, **76**(9), 1578, (1995)